Tailoring optical forces for nanoparticle manipulation on layered substrates

Mohammad M. Salary and Hossein Mosallaei*
Computational EM and Physics Lab, Electrical and Computer Engineering Department, Northeastern University, Boston, Massachusetts 02115, USA
(Received 13 February 2016; published 8 July 2016)

Optical forces can be used to manipulate small particles through various mechanisms. In this paper, we present a comprehensive analysis of optical forces acting on the nanoparticles located over a substrate using different manipulation techniques, as well as the conditions of the optimization of these forces. In particular, we study optical trapping, acceleration, and binding. Calculations are carried out using the exact multipole expansion method combined with Maxwell stress tensor formalism, providing a general framework to study optical forces on particles for arbitrary incident fields using closed-form expressions. The method takes into account multiple scattering between the particles and substrate and allows clear predictive abilities well beyond the dipole model. We consider the interaction of dielectric and metallic nanoparticles with various substrates. The presence of substrate is shown to have a significant impact on the nanoparticles' resonances and provides an additional degree of freedom in tailoring the optical forces. We explore different physical processes contributing to the optical force and their interplay on the mobility of the particle. It is established that engineering layered substrates can broaden the scope of trapping and acceleration and enhance the binding forces. It can also provide a high tunability of the acceleration direction. The analysis presented in this paper provides key physical insights to identify optimum setup for nanoparticles manipulation in various applications.

DOI: 10.1103/PhysRevB.94.035410

I. INTRODUCTION

The precise control and manipulation of micro- and nanoparticles is the key to a variety of applications and has been an active area of recent nanotechnology research. Numerous confinement and manipulation technologies have been developed over the years such as scanning tunneling microscope (STM) [1], atomic force microscopes (AFMs) [2], and transmission electron microscope (TEM) [3]. These technologies have been incorporated into nanolithography methods to fabricate micro- and nanostructures on metallic or semiconductor surfaces [4,5]. The main drawback of all scanning probe methods, however, remains that the interaction between the scanning probe and the substrate is controlled mechanically and that the probe is physically attached to a macroscopic scanning head or control unit.

One promising way for noncontact and noninvasive manipulation of micro- and nanoscale particles is to employ optical forces exerted by light upon its interaction with particles. Since the seminal work by Ashkin [6], optical forces have attracted significant attention and have been used for a variety of applications such as trapping and acceleration of nanoparticles [7–10], optical cooling [11], and sorting cells and biomolecules [12–14].

The physical mechanism of optical forces is based on momentum exchange between light and particles. It is well known that light carries a linear momentum associated with the wave vector. It can also carry an angular spin or orbit momentum where the former is dependent upon the polarization helicity and the latter depends on the phase structure of the light [15]. As the light interacts with a particle, there is an exchange between the momentum of light and the particle, which results in mechanical effects.

The optical forces may arise through different mechanisms and can be classified into two groups: nonconservative forces (due to radiation pressure and spin-orbit interactions) and conservative forces (gradient forces). The distinction between conservative and nonconservative forces is that the work done by conservative forces depends only on initial and final positions, while it is path-dependent for nonconservative forces. The conservative optical force is called gradient force and arises from the evanescent bonding between light waves. Inhomogeneities in the electric field intensity intrinsic to the structured light beams or created due to the scattering from other structures interacting with the incident field can result in a gradient force. Nonconservative force may arise due to exchange of linear momentum or an exchange between the spin and orbital parts of the angular momentum. The former effect is called radiation pressure, which is a result of scattering and absorption by the particle and the latter is a result of circular polarizability of the particle where the rotational symmetry is broken.

The strength and direction of optical forces depends strongly on the medium and particles optical properties, as well as on the parameters of the incident light. Several efforts have been put into finding the conditions under which the optically induced force is increased, as well as engineering its direction [16–25]. The majority of these works have been restricted to the particles suspended in a liquid or free space. However, from the applied point of view in many applications, we are interested in manipulation of the particles on a substrate for fabrication of nanoscale devices and forcing the particles into desired configurations [7–10].

Even though the optical force on particles above a substrate has been studied in specific cases [26–32], it has not been addressed in a rigorous analytic way. It is well established that the optical properties of a particle located over a substrate differ dramatically from those of the same particle in a homogeneous space. For short separations from substrate, the contribution from evanescent waves becomes dominant

*hosseinm@ece.neu.edu

as a result of multiple scattering and is not at all negligible. This consequently leads to the emergence of multipolar excitations and substrate-induced mode coupling and splitting. As such, Mie theory [26–28], ray optics [29], and dipolar analysis [30–32] are not applicable anymore and can lead to serious errors even for small Rayleigh particles [33]. For this purpose, numerical approaches have been used, which lack efficiency and are limited by memory size and computational time constraints [34–36].

In this paper, we use the exact multipole expansion method, taking into account the effect of multiple scattering between particles and substrate. Using the Maxwell stress tensor formalism, we arrive at closed-form expressions for optical forces acting onto the particles located over a substrate, which offers a significant advantage in calculation accuracy and efficiency. The method is very general, holding true for any arbitrary incident field, and does not invoke any simplifying assumptions. Owing to the high speed of the method, we present a comprehensive analysis of optical forces acting onto the nanoparticles located over a substrate in different manipulation techniques, as well as the conditions of the optimization of these forces. In particular, we study optical trapping, acceleration, and binding. The influence of different types of substrates on optical properties of dielectric and metallic nanoparticles is investigated, and it is shown how, by engineering layered substrates, optical forces can be tailored. We explore different physical processes contributing to the optical force and their interplay on the mobility of the particle. It is established that engineering layered substrates can broaden the scope of trapping and acceleration and enhance the binding forces. It can also provide high tunability for the acceleration direction. The results provide key physical insights on various interesting optical force phenomena. Understanding these effects will be instrumental for the development of self-organizing nanosystems in an optical field and optically driven fabrication technologies.

The paper is organized as follows. In Sec. II, we introduce the methods and formulation. The key equations are shown in this section, and the derivations and closed-form expressions for force components are provided in the Supplemental Material [37]. We investigate optical trapping of particles located over a substrate by incidence of a highly focused laser beam in Sec. III. Layered substrates are shown to be able to expand trapping regions of the particles in the resonant regime. In Sec. IV, tunable acceleration of a particle on substrate in two dimensions due to interplay of radiation pressure and spin-orbit coupling is illustrated by using oblique incidence of circularly polarized plane waves. Optical binding and the interparticle forces in a dimer placed on a substrate under illumination of plane waves are studied in Sec. V, and the role of surface plasmon polaritons (SPPs) and guided modes on enhancement of these forces is demonstrated. Finally, the conclusion is drawn in Sec. VI.

II. METHODS

A. Scattering from spherical particles on a layered substrate

Consider an array of N spherical particles located over a generic interface under illumination of an arbitrary incident field. The geometry of the problem is displayed in Fig. 1. Here, we have used the same approach of our previous work [38] on nanowires to extend the formulation for an array of spherical particles located over a layered substrate.

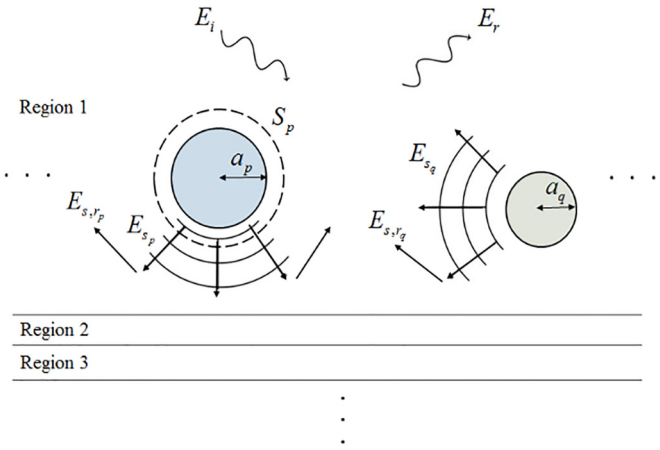

FIG. 1. Geometry of an array of particles located over a layered substrate under illumination of an arbitrary incident field. The arrows symbolize different field contributions involved in the scattering. The dashed line shows the surface across which the flux of Maxwell tensor is calculated for obtaining the optical force.

The total field in region 1 outside the particles can be written as the sum of four contributions: the incident field, the reflected field, the primary scattered field of the particles, and the secondary scattered field of the particles:

$$\mathrm{E}^{\mathrm{tot}} = \mathrm{E}^{i} + \mathrm{E}^{r} + \sum_{j=1}^{N} \mathrm{E}^{s,j} + \sum_{j=1}^{N} \mathrm{E}^{sr,j}. \tag{1}$$

The secondary scattered fields $\mathrm{E}^{sr,j}$ are due to the intrinsic substrate effect and are responsible for multiple scattering between the particles and substrate [39]. In this paper, we use an exact multipole expansion method to express all the field contributions in terms of vector spherical harmonics (VSHs) in the local coordinates of one particle. For pth particle, we have

$$\mathrm{E}^{\mathrm{tot},p} = \begin{bmatrix} \bar{a}_{mn}^{s,p} \\ \bar{b}_{mn}^{s,p} \end{bmatrix} \cdot \begin{bmatrix} \bar{\mathrm{M}}_{mn}^{(3)} \\ \bar{\mathrm{N}}_{mn}^{(3)} \end{bmatrix}^{t} + \left\{ \begin{bmatrix} \overline{a}_{mn}^{i,p} \\ \overline{b}_{mn}^{i,p} \end{bmatrix} + \begin{bmatrix} \overline{a}_{mn}^{r,p} \\ \overline{b}_{mn}^{r,p} \end{bmatrix} + \begin{bmatrix} \overline{a}_{mn}^{sr,p} \\ \overline{b}_{mn}^{sr,p} \end{bmatrix} + \sum_{\substack{q=1 \\ q\neq p}}^{N} \left(\begin{bmatrix} \overline{a}_{mn}^{s,qp} \\ \overline{b}_{mn}^{s,qp} \end{bmatrix} + \begin{bmatrix} \overline{a}_{mn}^{sr,qp} \\ \overline{b}_{mn}^{sr,qp} \end{bmatrix} \right) \right\} \begin{bmatrix} \overline{\mathrm{M}}_{mn}^{(1)} \\ \overline{\mathrm{N}}_{mn}^{(1)} \end{bmatrix}^{t}, \tag{2}$$

where $\overline{\mathrm{M}}_{mn}^{(l)}$ and $\overline{\mathrm{N}}_{mn}^{(l)}$ are the orthogonal VSHs of order l in the local coordinates of pth particle, $\overline{a}_{mn}^{i,p}, \bar{b}_{mn}^{i,p}$ and $\bar{a}_{mn}^{r,p}, \bar{b}_{mn}^{r,p}$ are the coefficients of incident and reflected field expansions in the local coordinates of pth particle, respectively, and

$$\begin{bmatrix} \overline{a}_{mn}^{s,qp} \\ \overline{b}_{mn}^{s,qp} \end{bmatrix} = \begin{bmatrix} \overline{\overline{A}}_{\mu\nu,mn}^{(3)}(R_{qp}) & \overline{\overline{B}}_{\mu\nu,mn}^{(3)}(R_{qp}) \\ \overline{\overline{B}}_{\mu\nu,mn}^{(3)}(R_{qp}) & \overline{\overline{A}}_{\mu\nu,mn}^{(3)}(R_{qp}) \end{bmatrix} \begin{bmatrix} \overline{a}_{mn}^{s,q} \\ \overline{b}_{mn}^{s,q} \end{bmatrix}, \tag{3}$$

$$\begin{bmatrix} \bar{a}_{mn}^{sr,qp} \\ \bar{b}_{mn}^{sr,qp} \end{bmatrix} = \begin{bmatrix} \bar{\bar{A}}^{(1)}_{\mu v,m'n'}(R_{qp}) & \bar{\bar{B}}^{(1)}_{\mu v,m'n'}(R_{qp}) \\ \bar{\bar{B}}^{(1)}_{\mu v,m'n'}(R_{qp}) & \bar{\bar{A}}^{(1)}_{\mu v,m'n'}(R_{qp}) \end{bmatrix} \cdot \begin{bmatrix} \bar{\bar{R}}^{11}_{m'n',mn} & \bar{\bar{R}}^{12}_{m'n',mn} \\ \bar{\bar{R}}^{21}_{m'n',mn} & \bar{\bar{R}}^{22}_{m'n',mn} \end{bmatrix} \begin{bmatrix} \bar{a}_{mn}^{s,q} \\ \bar{b}_{mn}^{s,q} \end{bmatrix}. \quad (4)$$

In the above equations, $\bar{\bar{A}}^{(l)}_{mn,\mu v}$, $\bar{\bar{B}}^{(l)}_{mn,\mu v}$ are translation coefficients of VSHs and $\bar{\bar{R}}^{ij}_{mn,m'n'}$ are the elements of substrate reflection matrix. $\bar{a}_{mn}^{s,j}$ and $\bar{b}_{mn}^{s,j}$ are the unknown scattered fields' coefficients of the particles, which can be obtained by solving the following system of equations:

$$\begin{bmatrix} \bar{\bar{\chi}}_{11} & \cdots & \bar{\bar{\chi}}_{1N} \\ \vdots & \vdots & \vdots \\ \bar{\bar{\chi}}_{N1} & \cdots & \bar{\bar{\chi}}_{NN} \end{bmatrix} \begin{bmatrix} \bar{a}_{mn}^{s,1} \\ \underline{\bar{b}_{mn}^{s,1}} \\ \vdots \\ \overline{\bar{a}_{mn}^{s,N}} \\ \bar{b}_{mn}^{s,N} \end{bmatrix} = \begin{bmatrix} \bar{a}_{mn}^{i,1} + \bar{a}_{mn}^{r,1} \\ \underline{\bar{b}_{mn}^{i,1} + \bar{b}_{mn}^{r,1}} \\ \vdots \\ \overline{\bar{a}_{mn}^{i,N} + \bar{a}_{mn}^{r,N}} \\ \bar{a}_{mn}^{i,N} + \bar{a}_{mn}^{r,N} \end{bmatrix}, \quad (5)$$

where diagonal elements of $\bar{\bar{\chi}}$ are given as

$$\bar{\bar{\chi}}_{ii} = \bar{\bar{T}}_p^{-1} - \begin{bmatrix} \bar{\bar{R}}^{11}_{mn,m'n'} & \bar{\bar{R}}^{12}_{mn,m'n'} \\ \bar{\bar{R}}^{21}_{mn,m'n'} & \bar{\bar{R}}^{22}_{mn,m'n'} \end{bmatrix}, \quad (6)$$

where $\bar{\bar{T}}_p$ is T matrix of pth particle, and the nondiagonal elements are

$$\bar{\bar{\chi}}_{ij} = -\begin{bmatrix} \bar{\bar{A}}^{(3)}_{mn,\mu v}(R_{ji}) & \bar{\bar{B}}^{(3)}_{mn,\mu v}(R_{ji}) \\ \bar{\bar{B}}^{(3)}_{mn,\mu v}(R_{ji}) & \bar{\bar{A}}^{(3)}_{mn,\mu v}(R_{ji}) \end{bmatrix} - \begin{bmatrix} \bar{\bar{A}}^{(1)}_{mn,\mu v}(R_{ji}) & \bar{\bar{B}}^{(1)}_{mn,\mu v}(R_{ji}) \\ \bar{\bar{B}}^{(1)}_{mn,\mu v}(R_{ji}) & \bar{\bar{A}}^{(1)}_{mn,\mu v}(R_{ji}) \end{bmatrix} \times \begin{bmatrix} \bar{\bar{R}}^{11}_{\mu v,\mu' v'} & \bar{\bar{R}}^{12}_{\mu v,\mu' v'} \\ \bar{\bar{R}}^{21}_{\mu v,\mu' v'} & \bar{\bar{R}}^{22}_{\mu v,\mu' v'} \end{bmatrix}. \quad (7)$$

The reader is referred to Sec. 1 of the Supplemental Material [37] for the notation and detailed derivation of the fields.

B. Optical forces acting onto spherical particles on a layered substrate

There are several ways for obtaining the optical forces, including the Lorentz force formalism [39,40], the Maxwell stress tensor method [41,42], and the decomposition into scattering and gradient forces [43,44]. The latter is widely used; however, it is applicable only for the limiting cases of the particle being small [45] or large [46] compared to wavelength. Here, we use the Maxwell tensor method, which can be applied to a high degree of accuracy for particles of arbitrary size and works well beyond the dipole model.

In general, the average force excreted upon a body by an electromagnetic wave can be calculated by evaluating the flux of the Maxwell stress tensor through a surface enclosing the scatterer:

$$\langle \mathrm{F} \rangle = \frac{1}{2} \mathrm{Re} \oint_S \bar{\bar{\mathrm{T}}}.\hat{n} dS, \quad (8)$$

where $\bar{\bar{\mathrm{T}}}$ is the Maxwell stress tensor, S is the surface enclosing the particle, and $\hat{n}$ is the unit vector normal to the surface. It should be emphasized that the results do not depend on the radius of the surface S and the center of the sphere selected for carrying the computations, as well as on the specific shape of the closed surface enclosing the particle. Actually, since the net force only depends upon the presence of scatterer, the closed surface can be chosen to lie entirely in region 1, as shown in Fig. 1.

The Maxwell stress tensor is defined as

$$\bar{\bar{\mathrm{T}}} = (\varepsilon_0 \varepsilon_r \mathrm{EE}^* + \mu_0 \mathrm{HH}^*) - \tfrac{1}{2}(\varepsilon_0 \varepsilon_r \mathrm{E}.\mathrm{E}^* + \mu_0 \mathrm{H}.\mathrm{H}^*)\bar{\bar{\mathrm{I}}}, \quad (9)$$

where ε_r stands for the relative permittivity of the background medium. The first two terms involve dyadic products, and $\bar{\bar{\mathrm{I}}}$ involved in the last two scalar products represents a 3×3 identity matrix. Given that the total field outside the particles written in (1), the nonvanishing force contributions on pth particle can be expressed as

$$\langle \mathrm{F}_p \rangle = \langle \mathrm{F}_{i,s_p} \rangle + \langle \mathrm{F}_{r,s_p} \rangle + \sum_{j=1}^{N} \left[\langle \mathrm{F}_{s_p,s_j} \rangle + \langle \mathrm{F}_{sr_j,s_p} \rangle \right], \quad (10)$$

where the force contributions have the following form:

$$\langle \mathrm{F}_{s_p,s_j} \rangle = \frac{1}{2} \mathrm{Re} \oint_{S_p} \begin{bmatrix} (\varepsilon_0 \varepsilon_r \mathrm{E}^{s,p} \mathrm{E}^{s,j^*} + \mu_0 \mathrm{H}^{s,p} \mathrm{H}^{s,j*}).\hat{r} \\ -\frac{1}{2}(\varepsilon_0 \varepsilon_r \mathrm{E}^{s,p} \mathrm{E}^{s,j^*} + \mu_0 \mathrm{H}^{s,p} \mathrm{H}^{s,j^*})\hat{r} \end{bmatrix} dS + \frac{1}{2} \mathrm{Re} \oint_{S_p} \begin{bmatrix} (\varepsilon_0 \varepsilon_r \mathrm{E}^{s,j} \mathrm{E}^{s,p^*} + \mu_0 \mathrm{H}^{s,j} \mathrm{H}^{s,p*}).\hat{r} \\ -\frac{1}{2}(\varepsilon_0 \varepsilon_r \mathrm{E}^{s,j} \mathrm{E}^{s,p^*} + \mu_0 \mathrm{H}^{s,j} \mathrm{H}^{s,p^*})\hat{r} \end{bmatrix} dS. \quad (11)$$

Similar expressions can be written for other force contributions. Note that in the calculation of $\langle \mathrm{F}_{s_p,s_p} \rangle$, only one of the above terms would be required.

Thanks to the exact method for solving the scattering problem and given that all the field contributions can be expressed in terms of VSHs of each particle, as written in (2), we are able to evaluate all the integrals analytically based on the method presented in [42], which results in analytical expressions for different force components. Closed-form expressions for force components and their detailed derivation are rather technical and are detailed in Sec. 2 of the Supplemental Material [37]. The convergence study of the method and important remarks regarding the implementation can also be found in the Supplemental Material [37] in Sec. 3 and Sec. 4, respectively.

This method is very general and is valid for any arbitrary incident field and all types of spherical particles and substrates. Moreover, because the vector spherical wave functions form an orthogonal complete basis, the method can be used to study scattering and forces on nonspherical particles as well. The closed-form expressions for optical forces not only offer a significant advantage in calculation accuracy and efficiency but also reveal the interactions between different contributions of the field.

In the following sections, we present a comprehensive study of optical forces acting onto the nanoparticles located over a substrate in different configurations. All the calculations reported on in this paper have been performed by an in-house computer code based on the presented method, which, to the best of our knowledge, has never been implemented for such a study.

III. OPTICAL TRAPPING

The trapping of nanoparticles has shown to be feasible at the high intensity regions of structured light beams by the action of gradient forces and is the heart of optical tweezer technologies [6]. One simple way to trap particles that can be integrated easily into compact lab-on-a-chip systems is to use highly focused laser beams with Gaussian intensity profile. In such an optical trap, the radiation pressure competes with gradient forces and tends to destabilize the particle confinement.

Both the gradient and scattering optical forces are shown to be strongest near the resonance. However, treatment of radiation pressure can be more complicated in the resonant regime and would likely limit trapping of particles. In the case of high-index particles in free space, there is an upper limit on the particle size that can be trapped stably due to strong scattering forces. For absorbing metallic particles, the radiation pressure also contains a contribution due to the light absorption, which causes difficulties in particle trapping even for tiny particle sizes. As such typical studies have been limited to polystyrene or silica particles in water (from 25 nm to 10 micrometers) or gold particles (10–250 nm) in wavelengths significantly far from the resonance wavelength [47,48].

In this section, we explore the possibility of trapping gold and silicon particles located over a substrate exposed by a Gaussian beam in the resonant regime. We study the resonant behavior of the particles and how, by engineering a layered substrate, stable trapping can be achieved.

The schematic of the configuration is shown in Fig. 2(a). The r is the radial coordinate defined as $r = \sqrt{x^2 + y^2}$. The beam center is placed on the substrate. The waist size is shown by w_0 and is related to the power of incident Gaussian beam by $P_0 = \pi |E_0|^2 w_0^2 / 4\eta_0$, with $\eta_0 = 377\ \Omega$ being the impedance of free space.

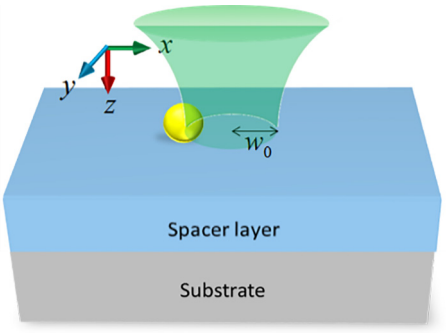

FIG. 2. The schematic configuration of the particle trapping using a highly focused laser beam. The particle is located over a substrate and is illuminated by a Gaussian beam with the waist of w_0.

In this paper, we consider gold and silicon particles whose trapping is proved to be more delicate. We fix the particles' size as $a = 90$ nm to bring out all the fundamental resonant modes in the visible light region. The refractive index of silicon is assumed to be 3.4, and the gold refractive index is taken from Johnson and Christy data [49]. The waist of the beam is set to $w_0 = 1\ \mu$m.

A Gaussian beam has a symmetric intensity profile in the radial direction with the maximum density at the center. The absolute value of the gradient force is maximal when the electric field gradient is maximal, where a typical Gaussian beam with waist of w_0 happens at radial distance of $w_0/2$ from the beam axis. The radial force becomes zero and changes sign at the beam axis, introducing an equilibrium position in the case of an attractive radial force. However, it is the axial force that is most important for determining whether a particle is trapped. In order to have a stable trapping, a repulsive force from substrate is required to lift the particle from the surface; otherwise, the trapping is not feasible due to a vanishing gradient force and an increasing frictional force as the particle moves toward the beam axis. Levitation of the particle from the substrate traps the particle in the equilibrium position above the substrate created by the interference of incident and reflected Gaussian beams [50].

When a Gaussian beam is reflected from the substrate, it forms a standing-wave pattern, and the particle can be confined in the intensity maximum of the interference fringe (antinode) above the substrate. However, when the particles are located on the substrate, the predominance of evanescent waves can give rise to more complex scattering patterns, which can pose challenges on trapping the particle. High optical intensity near the surface can cause the particles to be pushed toward the substrate by strong gradient forces. Moreover, the radial force can be turned repulsive as a result of scattering force arising from evanescent waves. Here, we show that the stable trapping in three dimensions can be achieved in the resonant regime by layered substrates and engineering resonances of the particle.

We start by inspecting the resonant behavior of the gold nanoparticle. Figures 3(a) and 3(b) show the extinction cross section of the particle on a silica and a gold substrate, respectively. The silica substrate does not introduce great distortions in the extinction spectrum of the particle. A

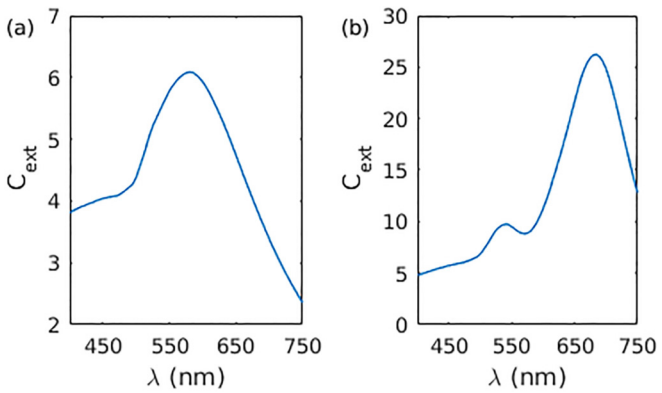

FIG. 3. Spectra of normalized extinction cross section of a gold nanoparticle with radius of 90 nm located over silica (a) and gold (b) substrates.

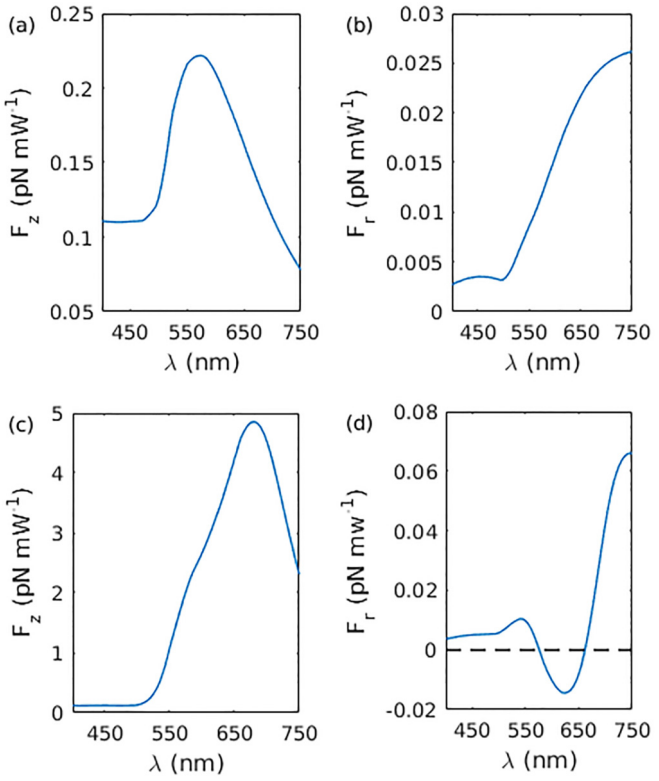

FIG. 4. Spectra of maximum axial (a, c) and radial (b, d) optical force exerted on the gold nanoparticle on silica (a, b) and gold (c, d) substrates.

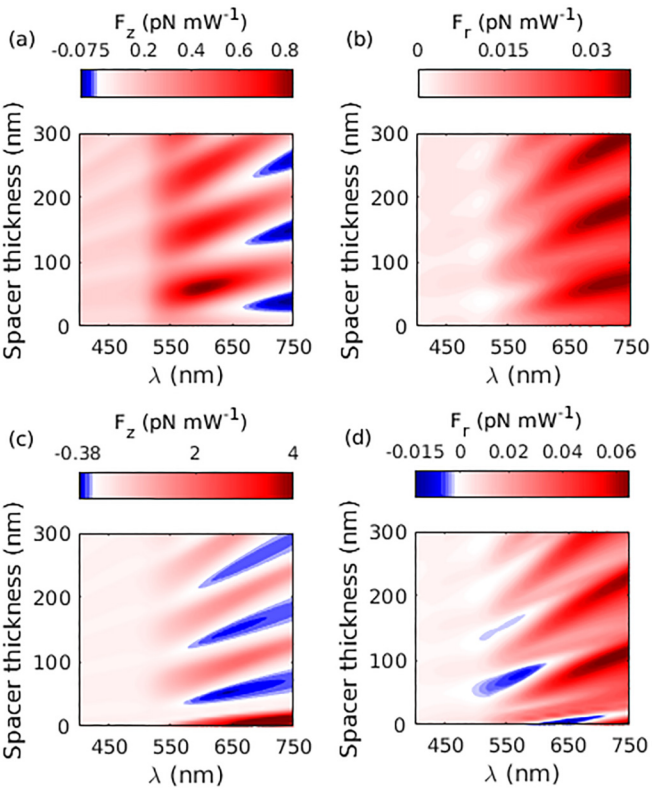

FIG. 5. The maximum axial (a, c) and radial (b, d) components of the optical force acting on the gold nanoparticle separated from silica (a, b) and gold (c, d) substrates by a silicon spacer layer, as a function of wavelength and spacer thickness. Blue and red colors represent attractive and repulsive forces, respectively.

resonant peak is observed at 580 nm, which corresponds to the localized surface plasmon (LSP) of the particle. Higher order peaks can also be observed outside the visible light range in lower wavelengths. Unlike the silica substrate, a gold substrate substantially changes the optical properties of the particle due to excitation of SPPs and propagating surface waves. As seen in Fig. 3(b), the extinction efficiency is greatly amplified as a result of strong coupling between the particle and substrate. The LSP resonance of the particle is redshifted to 684 nm. A second peak is also visible at 540 nm, which corresponds to the SPPs propagating on the gold-air interface and their reflection at the nanoparticle edges.

We calculate the optical force acting onto the particle using the closed-form formulas given in the Supplemental Material [37] [Eqs. (70)–(79)]. Before plotting the forces, the values are normalized to the source power. Figure 4 shows the maximum radial and axial components of the optical force for the silica (a, b) and gold (c, d) substrates. Several interesting features are noticed in the force plots. Directly at the LSP resonance, the radial force gets diminished while the axial force becomes maximum due to increased scattering. Approaching LSP resonance from the red-detuned side, the radial force peaks. The axial force at the LSP resonance on the gold substrate is significantly enhanced due to the coupling of the electromagnetic field between surface plasmons excited in gold nanoparticle and the antisymmetric image dipole formed in substrate. The peak corresponding to the SPP resonance is lacking on the axial force while it is observable for the radial force because the surface wave is traveling radially outward. The scattering force due to propagation of surface waves gives rise to a negative radial force by dominating over the diminished gradient forces around the LSP resonance. It is noteworthy that the origin of this repulsive radial force is a triumph of scattering force over gradient force, and it should be distinguished from a repulsive gradient force. A repulsive gradient force in a metallic particle occurs when the real part of polarizability changes sign [51], which is not the case for an 180-nm-sized gold nanoparticle (polarizability of the particle is never negative).

The strong coupling between the particle and the substrate leads to high intensities of evanescent waves in the vicinity of the substrate, which introduces a strong downward gradient force. In both cases of silica and gold substrates, the particle is subjected to a positive (attractive) axial force from the substrate at the whole range of wavelengths, which makes the trapping of the particle unfeasible.

The coupling strength of the particle and substrate is determined by the strength of the electric field driving the plasmonic resonance, which can be controlled by inserting a spacer layer between the particle and substrate. For this purpose, we introduce a silicon spacer layer with varying thickness between the particle and substrate, as shown in Fig. 2. Figure 5 depicts the maximum radial and axial components of the optical force versus wavelength and thickness of the silicon spacer layer for both silica (a, b) and gold (c, d) substrates.

Excitingly, we can now observe regions of negative axial force. This suggests that the particle can be trapped in these regions by choosing sufficient power to overcome other competing forces such as van der Waals (vdW) attraction and gravity. This effect is caused by constructive and destructive interference of the incident light reflected from the Silicon layer, resulting in strong variations in the driving field of the resonance, which changes direction of the axial gradient force, as follows from a simple interference model. Indeed, the oscillation periods found in Fig. 5 correspond to the additional phase shift of 2π for the light in the silicon layer (this is the half-wavelength of the light in silicon for the silica substrate). Higher reflectivity of gold substrate with respect to silica substrate results into a stronger repulsive axial force since the amplitudes of the incoming light and the light scattered from the Fabry-Pérot cavity compensate each other more. Repulsive radial forces can still be observed for the gold particle on a gold substrate at lower wavelengths due to dominance of scattering force caused by radially propagating guided modes. It should be noted that the same phenomena can be observed for a silica spacer. The only difference would be in the oscillations period and the value of the repulsive forces because of lower reflection.

This effect can be exploited to expand the trapping scope of gold nanoparticles into the resonant regime simply by the proper choice for the thickness of a spacer layer. It should be remarked that the expansion of the trapping scope is made possible by achieving a negative optical force, and the effect of other disruptive forces can be compensated by scaling the optical force magnitude through increasing the optical power of the source. In order to discuss relevance of our findings to experimental observations, we obtain trajectory of a gold particle in the presence of gravitational force, vdW attraction, and ambient damping of air, which simulates the trapping behavior in the experimental condition. We consider a gold nanoparticle with radius of $a = 90$ nm placed on a silicon layer with thickness of 55 nm backed by a gold substrate, illuminated by Gaussian beam with the waist of $w_0 = 1\ \mu$m at $\lambda = 650$ nm. Figure 6 depicts radial and axial components of the optical force acting onto the nanoparticle as a function of radial and axial displacement from the beam center. Equilibrium positions will be found at the intersections of white regions in the two plots.

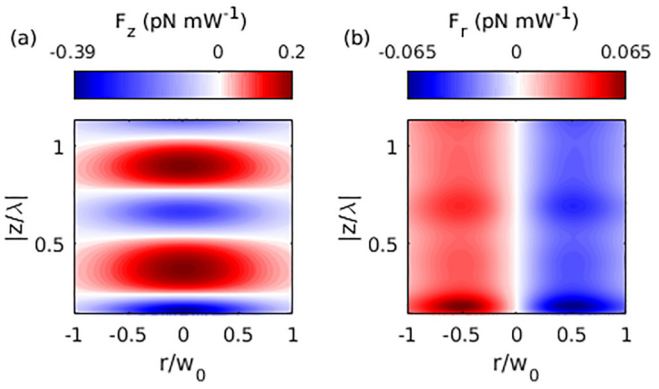

FIG. 6. The axial (a) and radial (b) optical force components on the gold particle versus the radial and axial displacement from the beam center. Blue and red colors represent attractive and repulsive forces, respectively.

The total force acting onto the particle is given by $\vec{F} = \vec{F}_{\text{light}} + mg\hat{z} + F_{\text{vdW}}\hat{z} - \gamma\vec{v} = m\frac{d\vec{v}}{dt}$, where $g = 9.8\,\text{m s}^{-2}$ is the gravitational constant and $m = 19320^{*}(4/3)\pi a^3$ kg is the mass of the particle. The ambient damping constant of air is given by $\gamma = 6\pi\mu a\,\text{kg s}^{-1}$, where $\mu = 1.84 \times 10^{-5}\,\text{kg m}^{-1}\,\text{s}^{-1}$ is the dynamic viscosity of dry air at room temperature. The vdW force is obtained from Lennard-Jones 6–12 potential [52] as $F_{\text{vdW}} = \frac{A_{12}d}{12z_0^2}$, where d is the distance between the particle and substrate, A_{12} is the Hamaker constant (for gold particle on silicon substrate $A_{12} = 1.27$ eV [52]), and z_0 is the position of the minimum of the Lennard-Jones potential, which is estimated at 0.5 nm. Note that when the particle is placed on the substrate, the vdW force is maximum, and $d = z_0$. It should be noted that in order to achieve a stable trapping, the ambient damping forces are necessary, and it has been shown that the particle cannot be trapped in vacuum [53].

The results in Fig. 6 suggest that in order to overcome the disruptive gravity and vdW forces, we need at least 450 μW for the source power. The trajectory of the particle is numerically solved by integrating Newton's equation for a source with $P_0 = 500\,\mu$W. Figure 7(a) shows the trajectory of the particle when the particle is initially located over substrate at radial distance of $w_0/2$ from the beam center. The time evolution of radial and axial displacements from the beam center is shown in Figs. 7(b) and 7(c), respectively. As can be seen, the stable trapping is achieved, and the particle is confined at the equilibrium position above the substrate.

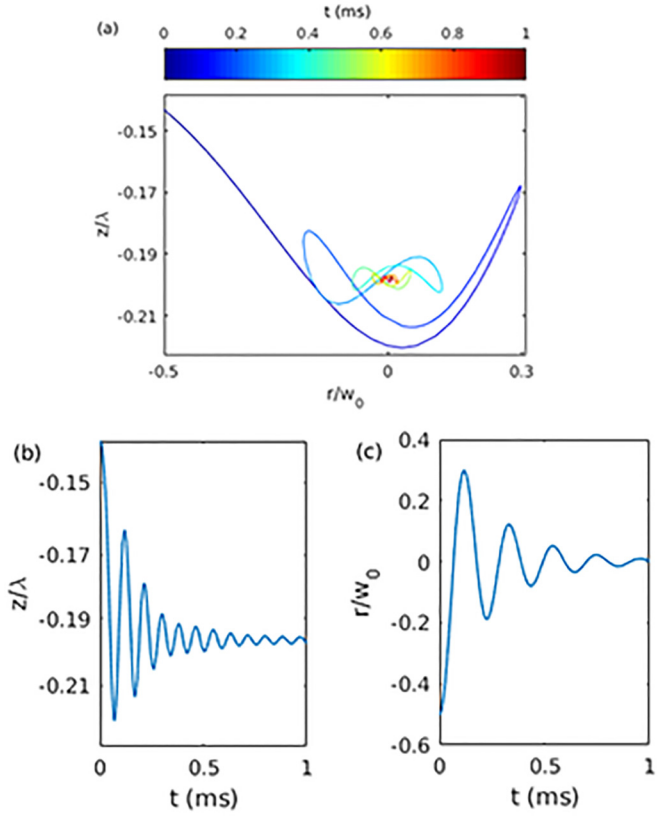

FIG. 7. Trajectory of the gold particle (a). Time evolution of axial (b) and radial displacement (c) of the particle from the beam center.

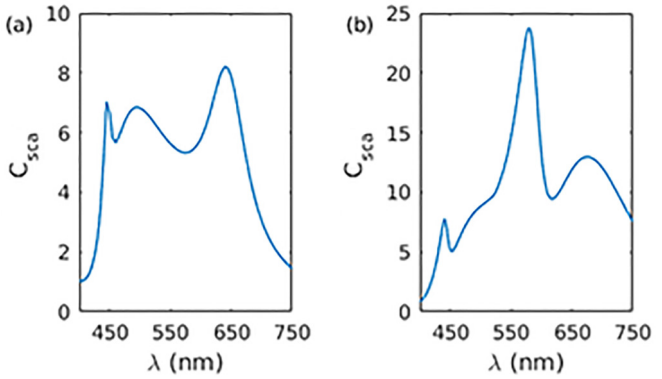

FIG. 8. Spectra of normalized scattering cross section of a silicon nanoparticle with radius of 90 nm located over silica (a) and gold (b) substrates in the visible light range.

It is important to note that when the particle is suspended in a fluid (liquid or gas), it is subject to the random Brownian motion [54]. The contribution of this randomness can be taken into account by writing the total force as $\vec{F} = \vec{F}_{\text{light}} + mg\hat{z} + F_{\text{vdW}}\hat{z} - \gamma\vec{v} - \sqrt{2k_BT\gamma}\eta(t)\hat{r} = m\frac{d\vec{v}}{dt}$, where k_B is the Boltzmann's constant, T is the temperature, and $\eta(t)$ is a white source noise (with a mean equal to zero $\langle\eta(t)\rangle = 0$). For the nanoparticles placed on a substrate in air at the room temperature ($k_BT = 0.025\,\text{eV} = 4 \times 10^{-21}\,\text{N m}^{-1}$), the value of $\sqrt{2k_BT\gamma}\eta(t)$ is in the order of 10^{-15}, which is negligible compared to the order of other terms in the equation (F_{light} is in order of 10^{-13}), and it does not affect the particle motion. However, the effect of Brownian motion can become more important at higher temperature or when the particles are placed in a liquid environment with higher ambient damping. In these cases, the stable zero-crossing of trajectory might need higher input powers.

We now turn to the trapping of a silicon particle located over a substrate. Figures 8(a) and 8(b) show the scattering cross sections of the particle on a silica and gold substrate, respectively. The silica substrate preserves the natural optical properties of the silicon particle. Three distinctive resonances are observed corresponding to magnetic quadrupole (MQ), electric dipole (ED), and magnetic dipole (MD) at 444 nm, 495 nm, and 640 nm, respectively. However, resonance modes and their optical response are strongly affected by the gold substrate and the excited propagating SPPs, in analogy with the case of gold nanoparticle. The ED resonance is split in two as the result of strong coupling between the SPP mode and the ED resonance of the particle. Moreover, the ED resonance becomes the strongest due to the retardation and the metal mirror image effect. The dipolar modes are amplified compared to the silica substrate except for the MQ resonance, which is suppressed.

The optical force excreted on the particle is obtained, and the results are shown in Fig. 9 for maximum radial and axial components of the force for both silica (a, b) and gold (c, d) substrates. Similar to the case of the gold particle, the axial forces become maximum at the resonances, and the radial forces peak in the red-detuned side of resonances. The axial force on a silica substrate is maximum at the MQ resonance, while interaction of higher order multipoles can lead to a

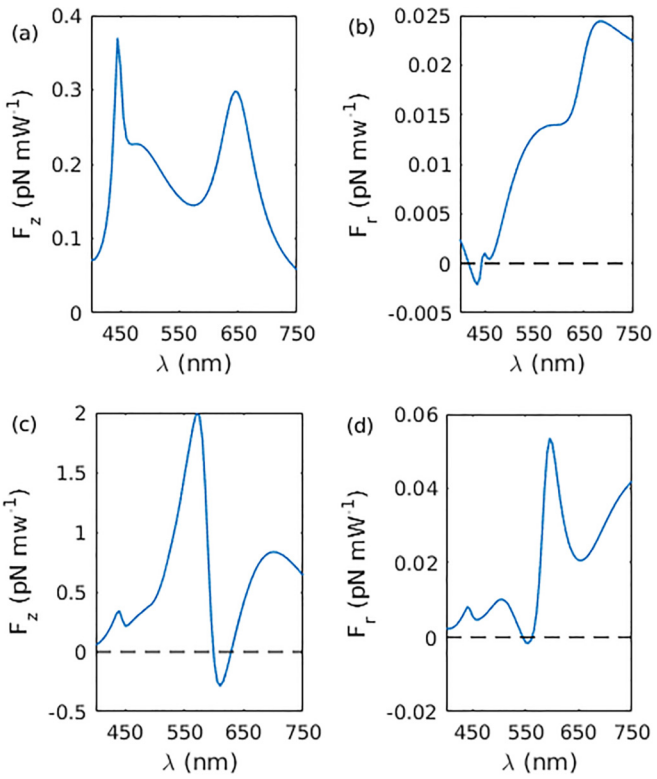

FIG. 9. The spectra of maximum axial (a, c) and radial (b, d) components of the optical force exerted on the silicon nanoparticle on silica (a, b) and gold (c, d) substrates.

negative radial force around this resonance. For the gold substrate, a third peak due to scattering force from SPPs is visible in the radial force plot at 504 nm [Fig. 9(d)], which is missing for the axial force. Moreover, the radial force can change to repulsive around this peak because of dominance of the scattering force over the gradient force. More interestingly, we observe a negative axial force around the MD resonance when the particle is placed on gold substrate, which is due to the interaction of the MD mode with its symmetric image in a gold substrate (as suggested by image theory, the force between a magnet and a metallic substrate is repulsive [55]). This allows us to trap the particle in this region with a greatly enhanced radial force.

Except for the narrow region for the gold substrate, the axial force is attractive at the other wavelengths, and the trapping is not feasible. This is due to the fact that high-index particles placed over a substrate are shown to exhibit a directional emission into the substrate, which gives rise to strong field intensity in the vicinity of the substrate and consequently an attractive gradient force. This forward scattering peaks at ED and MD resonances and is minimum at the wavelengths between these two resonances [56,57]. In a layered structure, the ratio of backward to forward scattering can be adjusted by changing thickness of the substrate. Hence, the same trapping scheme used for the gold particle can be used here to compensate the axial force by adding a silicon spacer layer with varying thickness between the particle and substrate. Figure 10 shows the maximum radial and axial components of the optical force for both silica (a, b) and gold (c, d) substrates.

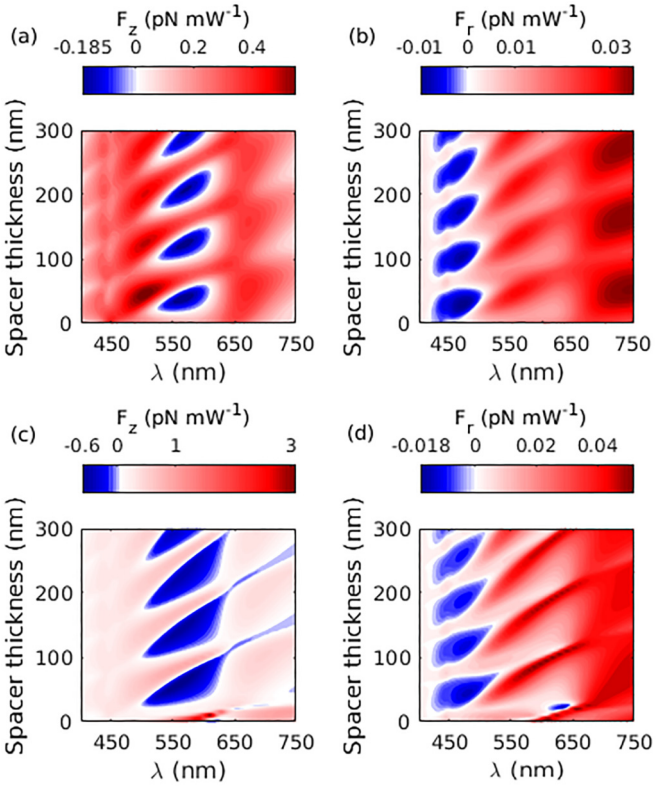

FIG. 10. The maximum axial (a, c) and radial (b, d) components of the optical force exerted on the silicon nanoparticle separated from silica (a, b) and gold (c, d) substrates by a silicon spacer layer, as a function of wavelength and spacer thickness.

As it can be seen, regions of negative axial force develop between ED and MD resonances where the forward scattering is minimum. This implies that the interference effects of the reflected field from the spacer layer can change direction of the gradient force to trap the particle between ED and MD resonances. For the gold substrate, narrow trapping regions are also observed around the MD resonance due to the interaction of MD with its symmetric image in the back mirror. Note that for both substrates, the radial force around MQ can become repulsive as a result of interaction between higher order multipoles. A negative deep is also present for the radial force on gold substrate around ED resonance where the thickness of spacer is small, which is attributed to the dominance of scattering force due to SPPs.

The proposed scheme offers a significant advantage to trap the particles in the repulsive axial force regions, exploiting the greatly enhanced radial force to our advantage at the same time. In order to illustrate interplay of different components of the force in the optical trapping, we obtain trajectory of the silicon particle in analogy to the case of gold nanoparticle. A silicon layer with thickness of 60 nm backed by a silica substrate is considered when the particle is illuminated by a Gaussian beam at 550 nm. The distribution of axial and radial components of the optical force in this case is shown in Fig. 11 versus radial and axial displacements from the beam center.

The mass of silicon particle can be obtained as $m = 2320^{*}(4/3)\pi a^3$ kg, and the Hamaker constant in the vdW force formula for a silicon particle on a silicon substrate is $A =$

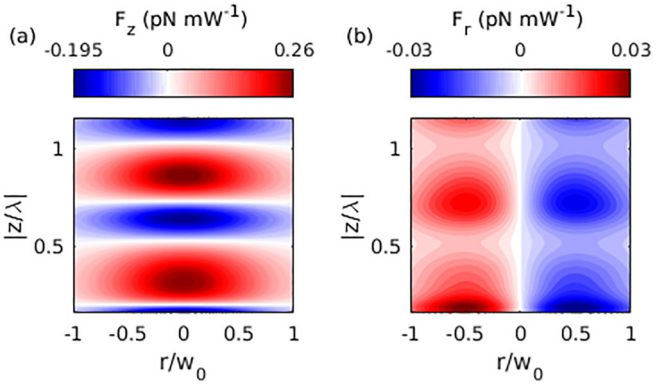

FIG. 11. The axial (a) and radial (b) components of the optical force acting on the silicon nanoparticle versus the radial and axial displacement from the beam center.

1.61eV [52]. The trajectory of the particle is shown in Fig. 12 alongside time evolution of axial and radial displacements from the beam center. As can be seen, trapping time is shorter compared to that of the gold particle, and the trajectory is smoother. This is because a silicon particle is ∼8 times lighter than a gold particle of the same size, and as a result the particle moves with a greater velocity.

In summary, this section presented a simple novel technique for expanding the scope of optical trapping of gold and silicon

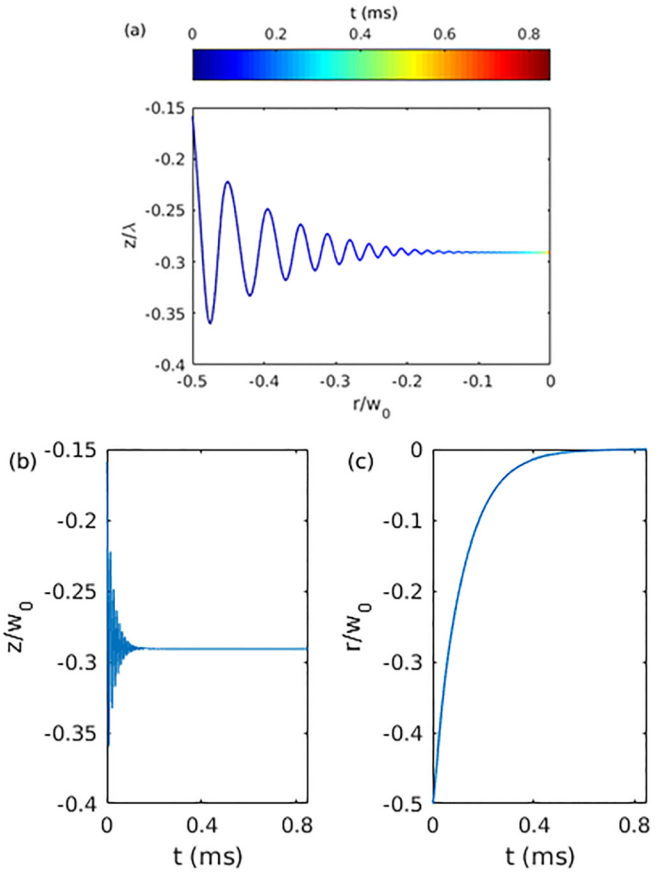

FIG. 12. (a) Trajectory of the silicon particle. Time evolution of axial (b) and radial (c) displacements of the particle from the beam center.

nanoparticles in the resonant regime using layered substrates, which offers low-power trapping of the particles.

IV. OPTICAL ACCELERATION

While optical tweezing techniques rely on structured light beams to move particles using gradient forces, radiation pressure can be used to accelerate and push particles. This can be done using a laser beam [6,10] or by a plane wave over a wide area of illumination [58]. However, radiation pressure acceleration is two dimensional and cannot manipulate the particle in the directions perpendicular to the plane of incidence. It has been recently proposed that the spin-orbit coupling can introduce another degree of freedom to push particles in lateral directions [58–62].

Spin-orbit coupling is a result of spin-Hall effect of light [63]. As a result of this effect, when light interacts with an object, there is an exchange between the spin and orbital parts of the angular momentum carried by the light. When the rotational symmetry is broken by an interface as a result of this interaction, the direction of the mechanical force is affected such that the conservation of canonical angular momentum is preserved.

This suggests that for a particle located over a substrate under illumination of an oblique circularly polarized plane wave, we can observe a lateral force component perpendicular to the incidence plane. This force can also arise when we have an oblique incidence of linear superposition of s- and p-polarized lights as the interference of reflected and incident waves in this configuration can result in a standing wave with elliptical polarization [58]. In fact, transforming between linear and circular polarization has been demonstrated by quarter-wave plates [64]. The difference between these two cases is that the circularly polarized incidence, while still affected by the reflected wave, does not rely on it to produce the lateral force. while the linear superposition of s and p polarizations rely on the interference of reflected and incident waves.

Recent theoretical investigations have unveiled lateral optical forces acting on the particles due to spin-orbit coupling in different configurations. While the force due to interference of the incident and reflected waves is nonvanishing only for large particles [59,60], it has been shown that contribution of guided modes and SPPs can enhance the lateral force and lead to a nonvanishing force for small particles [58].

In this section, we address the optical acceleration of particles located over a substrate through action of forces arising from radiation pressure and spin-orbit coupling by an obliquely incident circularly polarized plane wave. The method used in this paper takes into account the contribution of evanescent waves in addition to the lateral spin in the interference pattern of incident and reflected waves. We consider gold and silicon nanoparticles on different substrates to bring out the application-oriented physics and identify the optimal regions for optical acceleration. The dimensions of the particles were chosen as $a = 90$ nm, which were characterized in the previous section. The schematic configuration is shown in Fig. 13.

Assume that the wave vector is lying in the xz plane, as shown in Fig. 13. For a normal incidence, both F_x and F_y would be zero as both transverse and rotational symmetries

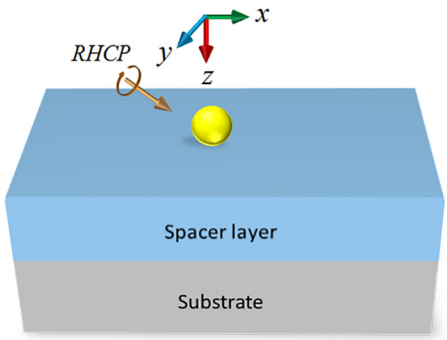

FIG. 13. A particle located over a substrate under illumination of an oblique circularly polarized plane wave. The wave vector is lying in the xz plane.

are preserved. With increasing of the incident angle, F_y starts to increase at first with occurrence of a lateral spin component and then decreases with increasing reflection. F_y would be also zero for slanted angles near 90°, as in this case $r_p = r_s = -1$, and interference of incident and reflected waves near the surface make light effectively linearly polarized, which makes the spin angular momentum of the total field to be zero. Here, we have assumed the incident angle to be 45° throughout this paper.

We begin by analyzing the force components acting on the gold particle placed over a substrate. Figure 14 depicts spectra of different components of the optical force for both right-handed (RH) and left-handed (LH) circular polarizations in the case of gold [14(a)–14(c)] and silica [14(b)–14(d)] substrates. The forces are normalized to the power density of the incident plane wave. F_x and F_z, which mainly represent radiation pressure, behave as expected and are maximum at the LSP resonance of the particle. A second peak is also observable for F_x when the SPPs are excited. This peak cannot be observed for F_z, which is because of the radial propagation of SPPs. In the case of F_y, unexpected features appear, which cannot be explained in terms of gradient and scattering forces. For one thing, when the circular polarization reverses, F_y reverses its direction, while F_x and F_z remain unchanged both in magnitude and in direction. This clearly shows the importance of circular polarization in the origin of this counterintuitive lateral force. F_y has the same order of magnitude as the transverse radiation pressure and even trumps over it around the LSP resonance when the particle is placed on the gold substrate. This is while for the dielectric substrate, the magnitude of this lateral force is significantly lower compared to the other components involved. This difference is attributed to the contribution of unidirectional SPPs excited by the particle on the gold substrate, while a dielectric half-space does not support any guided modes.

As seen in Fig. 14, when the particle is placed on the gold substrate, F_z is significantly larger compared to the force components along the substrate due to the strong coupling between surface plasmons excited in the gold nanoparticle and the antisymmetric image formed in substrate. This would likely limit the acceleration of the particle by introducing frictional forces. For the silica substrate, although F_z is not as great, F_y does not provide a high degree of freedom for acceleration in lateral directions.

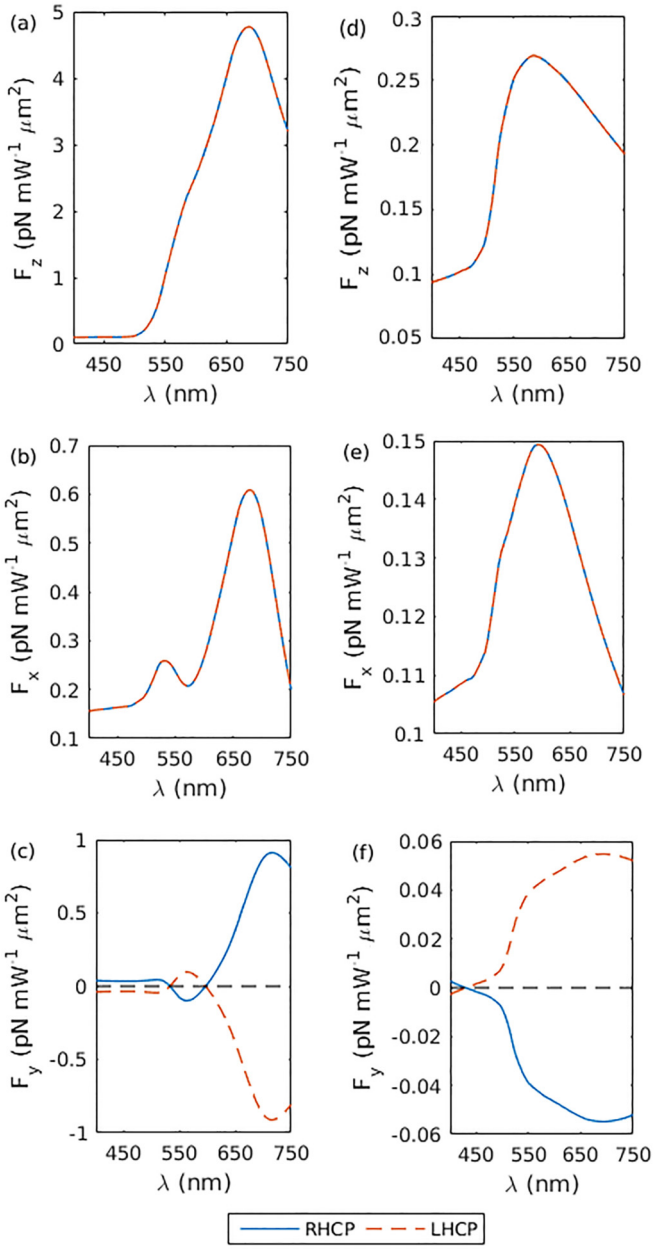

FIG. 14. The spectra of the optical force components acting on a gold nanoparticle with radius of 90 nm located over gold (a–c) and silica (d–f) substrates. The particle is illuminated by a circularly polarized plane wave with incident angle of 45°.

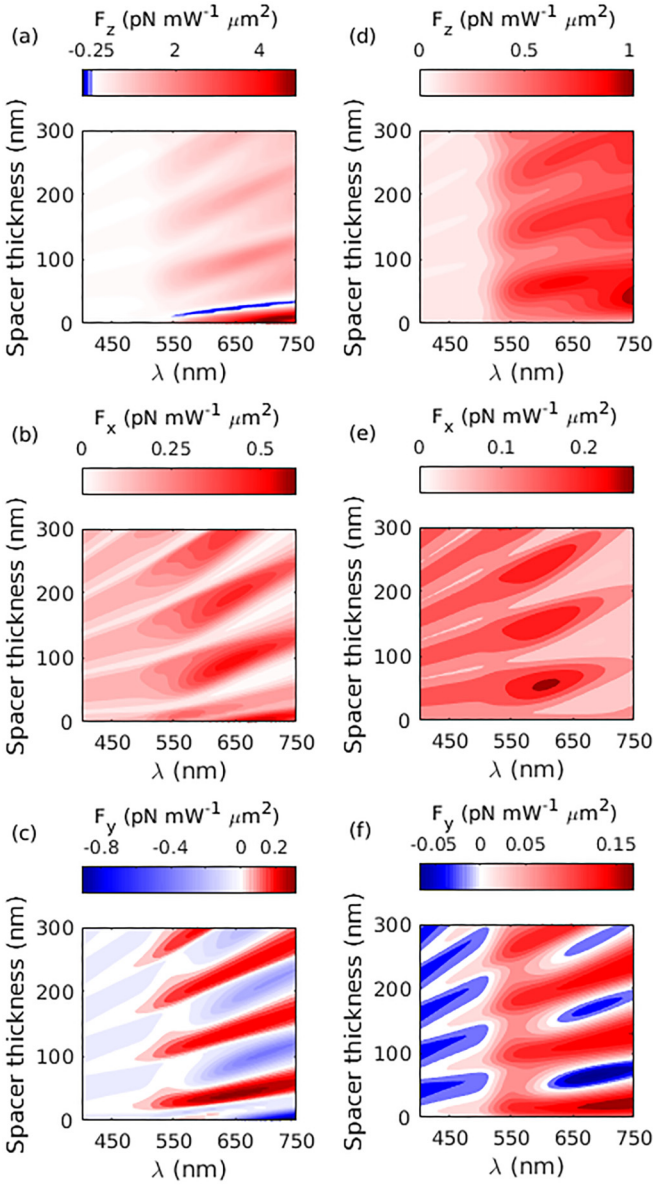

FIG. 15. The optical force components acting on the gold particle placed on a silicon layer with varying thickness backed by gold (a–c) and silica (d–f) substrates as a function of wavelength and silicon layer thickness. The particle is illuminated by a LH circularly polarized plane wave with incident angle of 45°.

To solve the abovementioned technical issues, we introduce a silicon spacer layer with varying thickness between the particle and substrate. This spacer layer can compensate the axial force on the gold substrate by controlling the coupling strength between the particle and substrate. It can also enhance the lateral force for the silica substrate by excitation of guided modes through internal reflections. As shown in Ref. [58] in the dipole-limit, transverse magnetic (TM) guided modes will have the dominant contribution to the lateral force. It should be noted that introducing the spacer layer will decrease the lateral force on the gold substrate by weakening of the coupling strength between the LSP and the SPPs.

Figure 15 depicts all the force components as a function of spacer layer thickness and wavelength for both gold [15(a)–15(c)] and silica [15(d)–15(f)] substrates for a LH circularly polarized incident plane wave with incident angle of 45°. Several interesting features can be observed. The axial force on the gold substrate is greatly compensated by introducing the spacer layer. Especially, a narrow repulsive region is observed around the SPP resonance, which is advantageous in terms of manipulation without the frictional forces introduced by F_z. F_x subsequently gets suppressed and enhanced as the thickness of spacer layer, and the driving field of the resonance varies. More interestingly, F_y exhibits an oscillatory behavior with Fabry-Pérot oscillations, which can lead to a change in the sign of this lateral force. This implies

that the direction of the acceleration can be tuned by changing the spacer layer thickness. The magnitude of F_y is greatly enhanced for the silica substrate due to excitation of TM guided modes. For the case of gold substrate, the maximum lateral force occurs when the particle is located over the substrate without the presence of spacer layer as a result of stronger interaction between LSP resonance and SPPs.

In order to clarify the results and discuss the interplay of different components of the force on the mobility of the particle, we obtain the initial acceleration of the particle and the lateral direction angle at which the particle accelerates as a function of wavelength and spacer layer thickness. The friction between the particle and the substrate is modeled as the static friction between two rigid bodies. It should be noted that after the initial static frictional phase, the particle can start to roll or slide over the substrate depending on the velocity of the particle and experimental conditions, which will affect the frictional forces [65]. Moreover, when the particle starts to move, the ambient damping and the resistance of air comes to the picture. These effects consequently change the acceleration of the particle. The static friction constant between a gold nanoparticle and a silicon substrate has been measured under different experimental conditions, and different values have been reported [66]. All the values lie in the range of 0.5–1. Here, we have considered a friction constant of 1; thus, these results should be viewed as a worst case scenario. The total force acting on the particle would be $\vec{F} = \vec{F}_{\text{light}} + mg\hat{z} + F_{\text{vdW}}\hat{z} - \mu_s(F_{z_{\text{light}}} + mg + F_{\text{vdW}})\hat{v}$, where μ_s is the friction constant. The relations for gravitational and vdW forces are given in the previous section. Note that although the frictional forces introduced by vdW and gravitational forces can be overcome by increasing the power, the friction introduced by F_z is inevitable. The results for the acceleration direction and magnitude are given at Fig. 16 for both gold 16(a), 16(b) and silica 16(c), 16(d) substrates for an incident power density of 10 mW μm^{-2}.

As can be seen, adding the spacer layer significantly expands the acceleration scope for the particle on gold substrate. Especially, higher accelerations can be achieved in the regions with a repulsive axial force. The results suggest that a wide control and tunability over direction is possible in the acceleration region by changing the spacer layer thickness. For the silica substrate, acceleration region will be limited to lower wavelengths off the resonance, while changing the spacer layer thickness can still provide additional degrees of freedom in direction of particle acceleration.

Here, we repeat the same study for the silicon nanoparticle. Different components of the optical force are shown versus the wavelength at Fig. 17 for both RH and LH circular polarizations for gold [17(a)–17(c)] and silica [17(b)–17(d)] substrates.

F_z and F_x show an expected behavior with their maximum being located at the resonances of the particle. F_y, however, exhibits intriguing features. Opposite forces emerge for opposite handednesses of circular polarization. The magnitude of F_y is comparable to other force components around ED and MD resonances when the particle is located on the gold substrate. This is attributed to the contribution of unidirectional SPPs. In fact, the ED and MD resonances of the silicon nanoparticle possess various photon wave vector components and can provide the appropriate momentum to excite gold

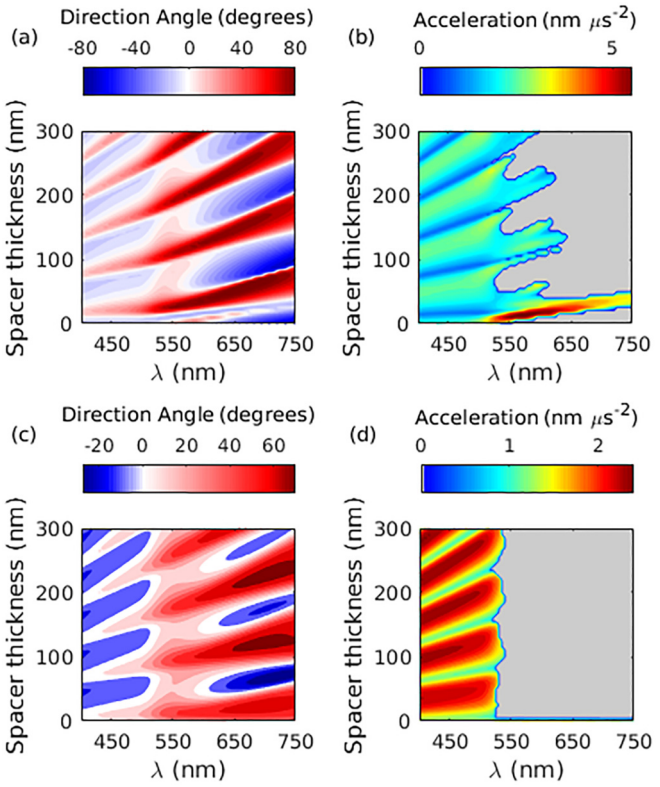

FIG. 16. The lateral direction angle and magnitude of optical acceleration for the gold particle located over gold (a, b) and silica (c, d) substrates. The shadowed regions represent nonmoving regions, where the frictional forces are dominated.

unidirectional SPPs. The magnitude of F_y on a dielectric substrate is considerably lower than the transverse radiation pressure as the substrate does not support any guided modes.

In analogy to the gold particle, the silicon particle suffers from the same limitations and challenges for acceleration, as the value of axial force on the gold substrate is significantly larger than other force components and the lateral force is small in the case of silica substrate.

In order to address these challenges and limitations, we investigate the optical forces on particles placed on a layered substrate. A silicon spacer layer is added between the particle and substrate. The effect on force components is studied by varying thickness. The force components are shown in Fig. 18 for both gold [18(a)–18(c)] and silica [18(d)–18(f)] substrates as a function of wavelength and spacer layer thickness for a LH circularly polarized incidence. As can be seen, the axial force in the case of gold substrate is greatly compensated, and repulsive axial forces develop between ED and MD resonances as the thickness of spacer layer varies. The axial force on the silica substrate is also greatly compensated between ED and MD resonances, while it is enhanced at the resonances. F_x gets subsequently suppressed and enhanced at the resonances with the change of spacer layer thickness. F_y is significantly increased for both silica and gold substrates around the MD resonance, which is due to the efficient coupling of MD resonances to TM guided modes supported by the silicon layer. Moreover, an oscillatory behavior is observed for F_y with the Fabry-Pérot oscillations in the spacer layer.

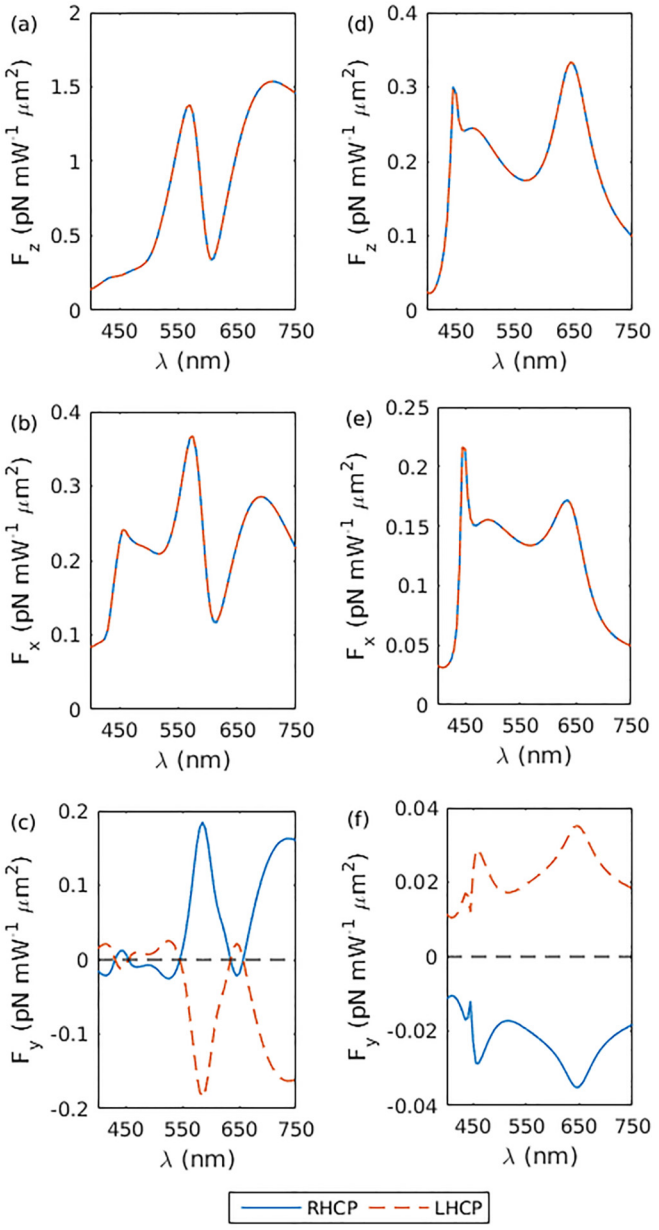

FIG. 17. The spectra of the optical force components acting on a silicon nanoparticle with radius of 90 nm located over gold (a–c) and silica (d–f) substrates. The particle is illuminated by a circularly polarized plane wave with incident angle of 45°.

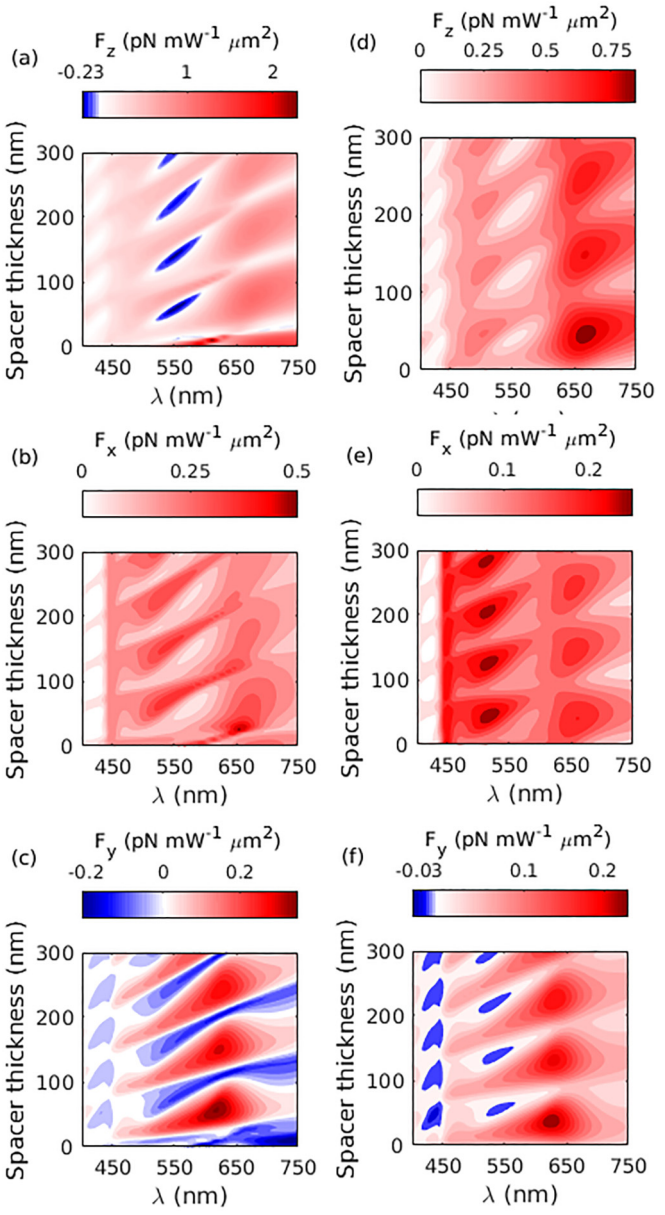

FIG. 18. The optical force components acting onto the silicon particle placed on a silicon layer backed by gold (a–c) and silica (d–f) substrates as a function of wavelength and silicon layer thickness. The particle is illuminated by a LH circularly polarized plane wave with incident angle of 45°.

In order to illustrate how the interplay of different components of the force affects the mobility of the particle and the advantages offered by the layered substrate, we obtain initial acceleration and its direction angle in analogy to the case of gold particle for an incident power density of 10 mW μm^{-2}. The results are shown in Fig. 19 for both gold 19(a), 19(b) and silica 19(c), 19(d) substrates. As can be seen, the acceleration scope is greatly expanded by introducing the spacer layer, especially for the case of gold substrate. In particular, we observe great accelerations between ED and MD resonances where the axial optical force is greatly compensated. This is accompanied by a great tunability in the acceleration direction for the gold substrate. In the case of silica substrate, F_x is mostly dominant over F_y in the acceleration regions, which limits the direction angle to smaller values.

In summary, this section showed two-dimensional acceleration of particles on substrate under action of forces due to radiation pressure and spin-orbit coupling. Layered substrates are shown to broaden acceleration scope of the particles and provide high degrees of tunability in the acceleration direction. Acceleration on a silica substrate is proved to be more challenging due to frictional forces introduced by F_z. It should be noted that the frictional forces introduced by the axial optical force cannot be compensated by increasing the power, and alternative methods should be investigated to expand the acceleration scope further.

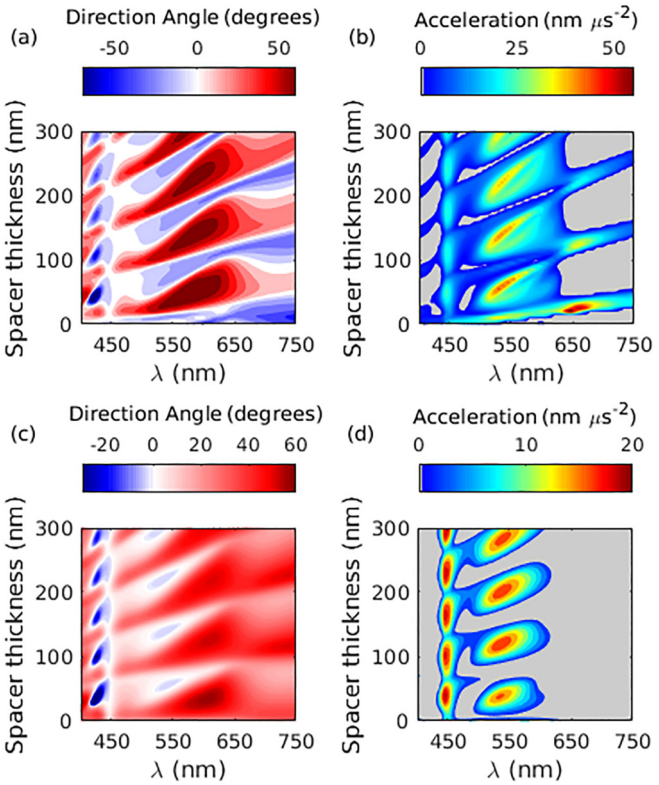

FIG. 19. The lateral direction angle and magnitude of optical acceleration for the silicon particle located over gold (a, b) and silica (c, d) substrates. The shadowed regions represent nonmoving regions, where the frictional forces are dominated.

V. OPTICAL BINDING

The idea of assembly of nanoparticles and forming aggregates using the interaction between them was first proposed in [67]. It has been shown that coupling between particles can induce either attractive or repulsive gradient forces. For small-sized particles in the nearfield (nonretarded coupling regime), the repulsive/attractive nature depends on the polarization of incident wave and subsequently the charge distribution on the particles [68–70].

In this section, we consider the interparticle forces in an identical gold dimer located over a substrate under illumination of a normal plane wave. In order to avoid retardation effects, the dimensions of the particles were chosen as $a_1 = a_2 = 25$ nm, which makes the particles ultrasubwavelength. The geometry of the configuration is shown in Fig. 20. The dimer axis is located on the x axis.

Figure 21 depicts the spectra of interparticle optical forces on different substrates when the particles are put at an edge-to-edge distance of 10 nm from each other, under illumination of parallel (a) and perpendicular (b) polarizations (with respect to the dimer axis). The forces are calculated for the LH side particle. Referring to Fig. 20, a positive force shows an attractive force between the particles, while a negative force is indicative of a repulsive force. The force on the other particle would have the opposite sign.

The interesting feature is that for all substrates, an attractive force is observed between the particles when the particles

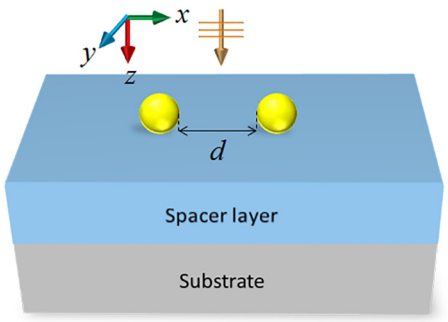

FIG. 20. The configuration of a gold dimer located over a substrate under illumination of normal plane wave. The dimer axis is located in the xz plane.

are illuminated with parallel polarization, and a repulsive force is observed when the incident wave has perpendicular polarization. This can be understood from distribution of induced charges on the particles. For parallel polarization, the induced charges on the edges of particles are asymmetric, which attract each other. This is the opposite for perpendicular polarization. Both repulsive and attractive forces peak in the magnitude at the resonance of the particle. Moreover, as seen in Fig. 21, both attractive and repulsive forces are greatly increased for the case of gold substrate (∼5 times compared to the free space), while the forces are slightly smaller on dielectric substrates with respect to the freestanding particles. The enhancement of the force on the gold substrate is directly attributed to the contribution of SPPs.

All of the optical force components acting on the first particle are studied as a function of wavelength and distance between the particles for both parallel and perpendicular polarization configurations when the particles are placed on the gold substrate. The results are shown in Fig. 22.

As seen in Fig. 22, both repulsive and attractive forces increase in magnitude when the distance between the particles decreases. For parallel polarization, forces are considerably stronger and increase at a greater rate as the particles approach each other. This is a direct consequence of the increasing field enhancement between the particles. At the same time, the spectral position of the force maximum redshifts due to

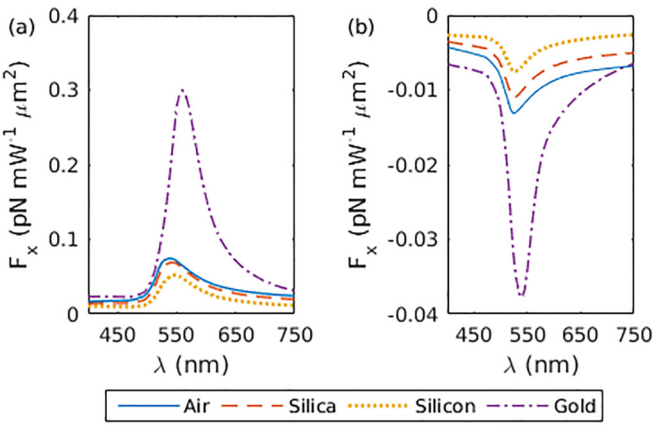

FIG. 21. Spectra of the optical force between two gold nanoparticles with radii $a1 = a2 = 25$ nm on different substrates for (a) parallel and (b) perpendicular polarization of incident wave.

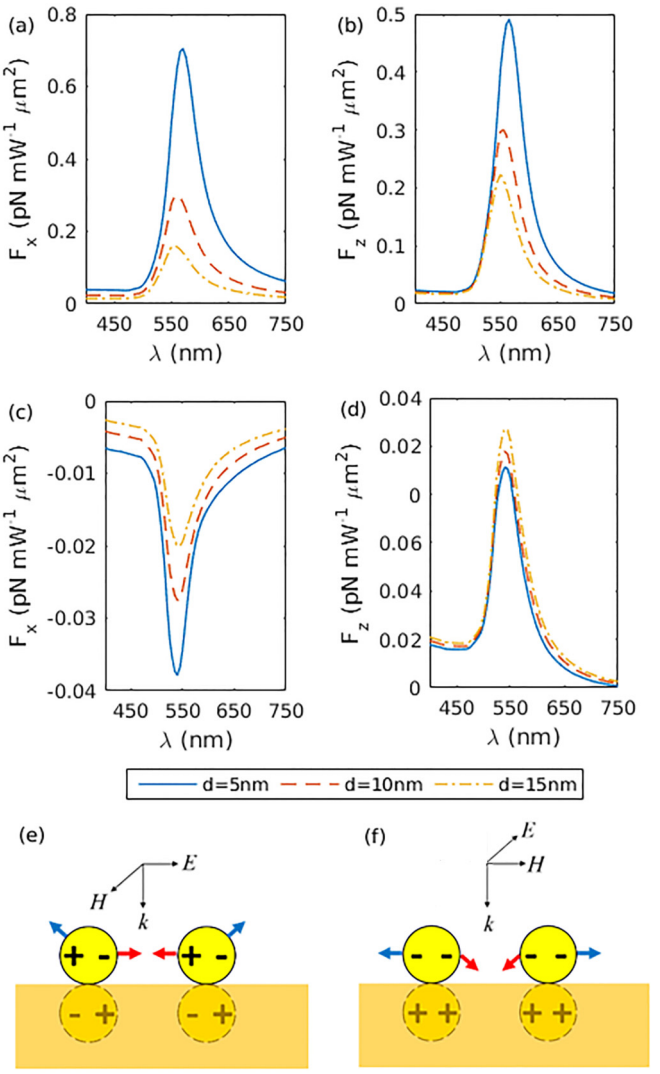

FIG. 22. Spectra of the optical force components acting on a gold nanoparticle located over a gold substrate in a dimer with different edge-to-edge distances for (a, b) parallel and (c, d) perpendicular polarization of incident wave. The distribution of induced charges on particles and their images in a metallic substrate in (e) parallel and (f) perpendicular polarizations.

plasmon hybridization [69]. Interestingly, the axial force has opposite trends versus distance for parallel and perpendicular configurations. In the case of parallel polarization, the axial force decreases as the particles move away from each other, while it increases with increasing distance for perpendicular polarization. This behavior is attributed to the interaction of the particle with the image of other particle in the substrate. As seen in Fig. 22(c), for parallel polarization configuration, the image of the other particle is symmetric, which gives rise to a repulsive force; as a consequence the axial force pointing toward the substrate decreases when the particles get closer to each other. For perpendicular polarization, the image is antisymmetric, which leads to an attractive force and consequently an increase in the axial force [Fig. 22(d)].

In order to discuss the interplay of different components of the optical force on the bonding and antibonding action, we plot the ratio of $|F_x/F_z|$ at the resonance, which can be

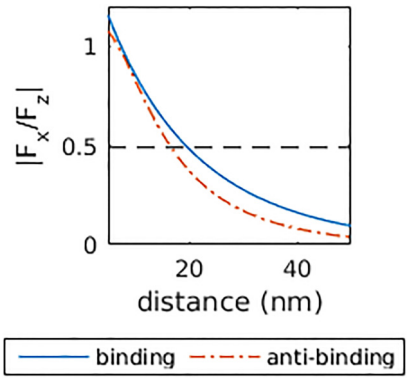

FIG. 23. The ratio of the interparticle force to the axial force in the gold dimer located over a gold substrate as a function of edge-to edge distance between the particles. The dashed line corresponds to the ratio of 0.49, which is the sliding friction constant between a gold body on a gold substrate.

regarded as a manifestation of the force needed to overcome frictional forces. As seen in Fig. 23, the ratio of $|F_x/F_z|$ decreases in both parallel and perpendicular polarization configurations as the distance increases. This implies that as the particles move away from each other, moving the particles with interparticle forces becomes more difficult. The dashed line in the figure corresponds to $|F_x/F_z| = 0.49$, which is the sliding friction constant of a gold body on a gold substrate. As the value of $|F_x/F_z|$ crosses this line, the movement would not be possible due to the frictional forces introduced by F_z. This suggests that the binding is possible for particles with distances up to 20 nm from each other, and separation is possible for distances up to 17 nm.

For optical binding, there is a competing repulsive vdW force between the particles. This force can be obtained as minus derivative of the London-vdW surface energy [52]. For equal-sized particles, it is defined as $\Phi = -\frac{A}{6}(\frac{4a^2}{s^2} + \frac{4a^2}{2(s^2-4a^2)} + \ln(1-\frac{4a^2}{s^2}))$, where A is Hamaker constant ($A = 4 \times 10^{-19}$ J for gold particles in vacuum [51]) and s is the distance between centers of the particles. The binding force at resonance and vdW force are shown as a function of edge-to-edge distance between the particles in Fig. 24. The

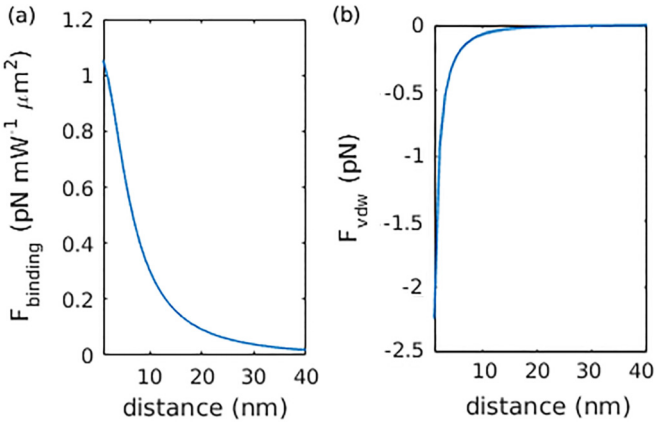

FIG. 24. (a) The binding force at the resonance and (b) the van der Waals force between two gold particles as a function of edge-to-edge distance.

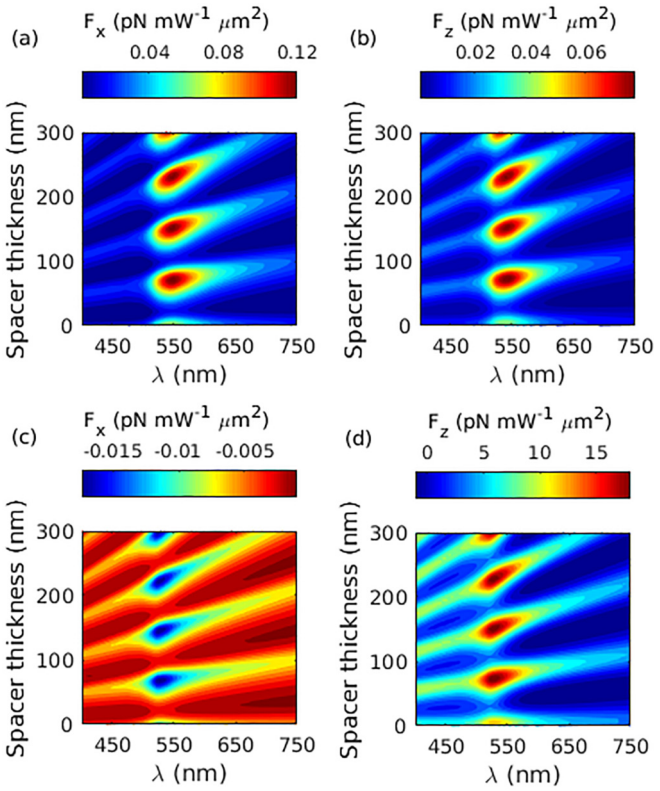

FIG. 25. The optical force components acting on a gold nanoparticle located over a silicon layer on a silica substrate in a dimer with edge-to-edge distance of 10 nm for (a, b) parallel and (c, d) perpendicular polarization of incident wave.

results imply that in order to overcome the vdW force, a minimum power of $\sim$2.25 mW μm^{-2} is required. Note that the slope of vdW force curve becomes very steep as the particles get very close to each other, and higher powers might be needed to make the particles contact with each other. It should be noted that the gravitational force between the two particles are in order of $\sim 10^{-30}$ N and clearly negligible.

In order to increase the interparticle forces on dielectric substrates, it is advantageous to use a layered structure, as they support guided modes that can enhance these forces in analogy to the contribution of SPPs. For this purpose, a silicon spacer layer with varying thickness is added between the particles and a silica substrate. The results are shown in Fig. 25 for parallel (a, b) and perpendicular (c, d) polarizations when the particles are separated by an edge-to-edge distance of 10 nm. As can be seen, both attractive and repulsive forces are increased significantly by adding the spacer layer. This allows us to overcome competing vdW forces with lower input power.

Finally, it should be noted that for silicon particles of the same size, similar behavior is observed while the interparticle forces are weaker comparing to the gold dimer. This is because gold dimers are more strongly coupled due to LSPs. The above force properties are for identical dimers in the nonretarded regime. As the particle size increases, retardation effects start to appear, which can make the case complicated. Moreover, on nonidentical dimers, higher order modes can be excited, and the force can be repulsive or attractive irrespective of polarization configuration. Studying optical forces on more complex clusters of nanoparticles would enable the mass movement, arrangement, and sorting of particles and requires further investigations, which remains the topic of our future research.

VI. CONCLUSIONS

In conclusion, we presented a comprehensive analysis of different components of the optical force associated with various manipulation techniques using an analytical approach. We demonstrate the advantages of layered substrates in different manipulation techniques and the way they can be employed to tailor optical forces. Engineering the substrate is shown to broaden the scope of particle trapping and acceleration and to enhance the binding forces. Moreover, it can provide high degrees of tunability in the acceleration direction. Optimum regions for optical manipulation of gold and silicon particles located over different substrate are identified, and the relevance of the results to experimental observations is discussed in detail. The analytical formulation implemented is general and can be readily utilized for complex aggregates of the particles located over a substrate under illumination of arbitrary structured light beams and paves the way to study and address the challenges of nanoparticles manipulations with optical forces.

ACKNOWLEDGMENTS

This paper is supported by DARPA award (via Grant No. N00014-14-1-0850). The authors would like to acknowledge the helpful discussions with Sandeep Inampudi.

[1] G. Binnig, H. Rohrer, Ch. Gerber, and E. Weibel, Phys. Rev. Lett. **49**, 57 (1982).
[2] G. Binnig, C. Quate, and Ch. Gerber, Phys. Rev. Lett. **56**, 930 (1986).
[3] D. Williams and C. Carter, *Transmission Electron Microscopy* (Springer, New York, 2009).
[4] A. Tseng, A. Notargiacomo, and T. Chen, J. Vac. Sci. Technol. B **23**, 877 (2005).
[5] R. Garcia, A. Knoll, and E. Riedo, Nat. Nanotech. **9**, 577 (2014).
[6] A. Ashkin, Phys. Rev. Lett. **24**, 156 (1970).
[7] V. G. Shvedov, A. V. Rode, Y. V. Izdebskaya, A. S. Desyatnikov, W. Krolikowski, and Y. S. Kivshar, Phys. Rev. Lett. **105**, 118103 (2010).
[8] S. Nedev, A. Urban, A. Lutich, and J. Feldmann, Nano Lett. **11**, 5066 (2011).
[9] O. Maragò, P. Jones, P. Gucciardi, G. Volpe, and A. Ferrari, Nat. Nanotech. **8**, 807 (2013).
[10] M. Fedoruk, M. Meixner, S. Carretero-Palacios, T. Lohmüller, and J. Feldmann, ACS Nano **7**, 7648 (2013).
[11] W. Phillips, Rev. Mod. Phys. **70**, 721 (1998).

[12] A. Ashkin and J. Dziedzic, Science **235**, 1517 (1987).
[13] S. Sato and H. Inaba, Opt. Quantum Electron. **28**, 1 (1996).
[14] Y. Pang, H. Song, J. Kim, X. Hou, and W. Cheng, Nat. Nanotech. **9**, 624 (2014).
[15] L. Allen, S. Barnett, and M. Padgett, *Optical Angular Momentum* (Institute of Physics Pub., Bristol, 2003).
[16] N. Simpson, D. McGloin, K. Dholakia, L. Allen, and M. Padgett, J. Mod. Opt. **45**, 1943 (1998).
[17] S. Reihani and L. Oddershede, Opt. Lett. **32**, 1998 (2007).
[18] Y. Hu, T. Nieminen, N. Heckenberg, and H. Rubinsztein-Dunlop, J. Appl. Phys. **103**, 093119 (2008).
[19] M. Mahamdeh, C. Pérez Campos, and E. Schäffer, Opt. Express **19**, 11759 (2011).
[20] K. Dholakia and T. Čižmár, Nat. Photon. **5**, 335 (2011).
[21] M. Padgett and R. Bowman, Nat. Photon. **5**, 343 (2011).
[22] J. Glückstad, Nat. Photon. **5**, 7 (2011).
[23] A. Jannasch, A. Demirörs, P. van Oostrum, A. van Blaaderen, and E. Schäffer, Nat. Photon. **6**, 469 (2012).
[24] O. Brzobohatý, V. Karásek, M. Šiler, L. Chvátal, T. Čižmár, and P. Zemánek, Nat. Photon. **7**, 123 (2013).
[25] C. Pfeiffer and A. Grbic, Phys. Rev. B **91**, 115408 (2015).
[26] E. Almaas and I. Brevik, J. Opt. Soc. Am. B **12**, 2429 (1995).
[27] A. Jonáš, P. Zemánek, and E. Florin, Opt. Lett. **26**, 1466 (2001).
[28] P. Jákl, M. Šerý, J. Ježek, A. Jonáš, M. Liška, and P. Zemánek, J. Mod. Opt. **50**, 1615 (2003).
[29] J. Walz, Appl. Opt. **38**, 5319 (1999).
[30] A. Shalin, Phys. Met. Metallogr. **112**, 36 (2011).
[31] C. Van Vlack, P. Yao, and S. Hughes, Phys. Rev. B **83**, 245404 (2011).
[32] S. Wang and C. Chan, Opt. Express **24**, 2235 (2016).
[33] J. Arias-González and M. Nieto-Vesperinas, Opt. Lett. **27**, 2149 (2002).
[34] M. Lester and M. Nieto-Vesperinas, Opt. Lett. **24**, 936 (1999).
[35] P. C. Chaumet and M. Nieto-Vesperinas, Phys. Rev. B **61**, 14119 (2000).
[36] P. C. Chaumet, A. Rahmani, and M. Nieto-Vesperinas, Phys. Rev. B **66**, 195405 (2002).
[37] See Supplemental Material at http://link.aps.org/supplemental/10.1103/PhysRevB.94.035410 for more details regarding the formulation and remarks on the convergence and technical implementation of the method.
[38] M. Salary, M. Nazari, and H. Mosallaei, J. Opt. Soc. Am. B **32**, 2448 (2015).
[39] J. Lermé, C. Bonnet, M. Broyer, E. Cottancin, D. Manchon, and M. Pellarin, J. Phys. Chem. C **117**, 6383 (2013).
[40] M. Mansuripur, Opt. Express **12**, 5375 (2004).
[41] J. Barton, D. Alexander, and S. Schaub, J. Appl. Phys. **66**, 4594 (1989).
[42] A. Salandrino, S. Fardad, and D. Christodoulides, J. Opt. Soc. Am. B **29**, 855 (2012).
[43] A. Rohrbach and E. Stelzer, J. Opt. Soc. Am. A **18**, 839 (2001).
[44] P. Hansen, V. Bhatia, N. Harrit, and L. Oddershede, Nano Lett. **5**, 1937 (2005).
[45] A. Ashkin and J. Gordon, Opt. Lett. **8**, 511 (1983).
[46] A. Ashkin, Biophys. J. **61**, 569 (1992).
[47] P. M. Bendix, L. Jauffred, K. Norregaard, and L. B. Oddershede, IEEE J. Select. Topics Quantum Electron. **20**, 15 (2014).
[48] A. Jonáš and P. Zemánek, Electrophoresis **29**, 4813 (2008).
[49] P. Johnson and R. Christy, Phys. Rev. B **6**, 4370 (1972).
[50] P. Zemánek, A. Jonáš, and M. Liška, J. Opt. Soc. Am. A **19**, 1025 (2002).
[51] M. Dienerowitz, M. Mazilu, P. Reece, T. Krauss, and K. Dholakia, Opt. Express **16**, 4991 (2008).
[52] J. Visser, Adv. Colloid Interface Sci. **3**, 331 (1972).
[53] N. Wang, J. Chen, S. Liu, and Z. Lin, Phys. Rev. A **87**, 063812 (2013).
[54] K. Dholakia, P. Reece, and M. Gu, Chem. Soc. Rev. **37**, 42 (2008).
[55] L. Shi, E. Xifré-Pérez, F. García de Abajo, and F. Meseguer, Opt. Express **20**, 11247 (2012).
[56] J. van de Groep and A. Polman, Opt. Express **21**, 26285 (2013).
[57] I. Staude, A. Miroshnichenko, M. Decker, N. Fofang, S. Liu, E. Gonzales, J. Dominguez, T. Luk, D. Neshev, I. Brener, and Y. Kivshar, ACS Nano **7**, 7824 (2013).
[58] F. Rodríguez-Fortuño, N. Engheta, A. Martínez, and A. Zayats, Nat. Commun. **6**, 8799 (2015).
[59] A. Y. Bekshaev, K. Y. Bliokh, and F. Nori, Phys. Rev. X **5**, 011039 (2015).
[60] K. Bliokh, A. Bekshaev, and F. Nori, Nat. Commun. **5**, 3300 (2014).
[61] S. Sukhov, V. Kajorndejnukul, R. Naraghi, and A. Dogariu, Nat. Photon. **9**, 809 (2015).
[62] M. Alizadeh and B. Reinhard, ACS Photon. **2**, 1780 (2015).
[63] K. Bliokh, D. Smirnova, and F. Nori, Science **348**, 1448 (2015).
[64] Y. Zhao and A. Alù, Phys. Rev. B **84**, 205428 (2011).
[65] H. Xie, *Atomic Force Microscopy Based Nanorobotics* (Springer, Berlin, 2011).
[66] S. Darwich, K. Mougin, A. Rao, E. Gnecco, S. Jayaraman, and H. Haidara, Beilstein J. Nanotechnol. **2**, 85 (2011).
[67] M. M. Burns, J.-M. Fournier, and J. A. Golovchenko, Phys. Rev. Lett. **63**, 1233 (1989).
[68] R. Nome, M. Guffey, N. Scherer, and S. Gray, J. Phys. Chem. A **113**, 4408 (2009).
[69] V. Miljković, T. Pakizeh, B. Sepulveda, P. Johansson, and M. Käll, J. Phys. Chem. C **114**, 7472 (2010).
[70] Q. Zhang, J. Xiao, X. Zhang, and Y. Yao, Opt. Commun. **301–302**, 121 (2013).